Geochemistry, Geophysics, Geosystems

RESEARCH ARTICLE
10.1029/2017GC007322

Effects of Confinement on Reaction-Induced Fracturing During Hydration of Periclase

Xiaojiao Zheng[1], Benoît Cordonnier[1,2], Wenlu Zhu[3], François Renard[1,4], and Bjørn Jamtveit[1]

[1]The Njord Centre, Physics of Geological Processes, Department of Geosciences, University of Oslo, Oslo, Norway, [2]ESRF – The European Synchrotron, Grenob1e, France, [3]Department of Geology, University of Maryland, College Park, MD, USA, [4]Université Grenoble Alpes, Université Savoie Mont Blanc, CNRS, IRD, IFSTTAR, ISTerre, Grenoble, France

Abstract Hydration of a nominally dry rock can cause expansion of the solid volume, resulting in reaction-induced fracturing and an associated increase in the porosity and permeability of the rock. We study the effect of confinement on the coupling between stress generation, reaction-induced fracturing, and porosity evolution during the hydration of periclase (MgO) into brucite ($Mg(OH)_2$). Samples of a microporous MgO ceramic were hydrated at 170–210 °C, 5–80 MPa confining pressure, 6–95 MPa differential stress, and 5–75 MPa pore fluid pressure in a purpose-designed triaxial load cell. Hydration-induced changes were recorded in situ by X-ray microtomographic imaging at 5-min intervals. Below 30 MPa effective mean stress, the fraction of periclase replaced by brucite is a sigmoidal function of time. After a slow start, the replacement rate picks up with concomitant intense fracturing. The porosity increase resulting from the reaction-induced fractures is transient (pulse-like). Following the porosity pulse the rate of replacement declines until the replacement is almost complete. Above 30 MPa, the reaction rate is slow, porosity decreases monotonically without any observable fracturing during the time of the experiment. At these stress conditions, the lack of fracturing cannot be limited by the thermodynamic affinity of the reaction. A possible interpretation is that the stress generated by the reaction may overcome the disjoining pressure at the grain-grain interface, expelling the water film trapped there and thereby dramatically reducing the reaction rate.

Key Points:
- Time-resolved in situ X-ray microtomography allows imaging of reaction-induced fracturing
- Reaction-induced fracturing is associated with a transient porosity pulse
- Reaction-induced fracturing slows down considerably when the effective mean stress exceeds a certain threshold

Supporting Information:
- Supporting Information S1
- Movie S1
- Movie S2

Correspondence to:
X. Zheng,
xiaojiao@geo.uio.no

Citation:
Zheng, X., Cordonnier, B., Zhu, W., Renard, F., & Jamtveit, B. (2018). Effects of confinement on reaction-induced fracturing during hydration of periclase. *Geochemistry, Geophysics, Geosystems*, *19*, 2661–2672. https://doi.org/10.1029/2017GC007322

Received 3 NOV 2017
Accepted 19 JUN 2018
Accepted article online 26 JUL 2018
Published online 18 AUG 2018

1. Introduction

Reaction-induced fracturing is a common phenomenon in both natural and man-made materials. Salt growth in building materials such as rocks and cements is a major problem that causes serious deterioration and weakening of man-made structures (Scherer, 1999). In geological systems, reaction-induced fracturing (MacDonald & Fyfe, 1985; O'Hanley, 1992) occurs in a variety of situations, ranging from weathering to retrograde metamorphism, where volatilization reactions (especially hydration or carbonation) and mineral precipitation result in a local increase in solid volume (Fletcher et al., 2006; Gratier et al., 2012; Jamtveit et al., 2008, 2009; Jamtveit & Hammer, 2012; Kelemen et al., 2011; Kelemen & Hirth, 2012; Kelemen & Matter, 2008; Malvoisin et al., 2017; Noiriel et al., 2010; Rudge et al., 2010; Ulven, Jamtveit, & Malthe-Sørenssen, 2014; Ulven, Storheim, et al., 2014).

Since growth and/or swelling in a porous material will tend to clog initially connected porosity (Hövelmann et al., 2012) and thus reduce the permeability, reaction-induced fracturing (Zhu et al., 2016) is thought to be critical in sustaining fluid-induced reactions in a system that otherwise would become impermeable to the influx of external fluids. Whether reaction-induced fracturing occurs has far-reaching consequence for a number of applications including the feasibility of capturing CO_2 through reactions involving ultramafic rocks (Kelemen et al., 2011; Oelkers et al., 2008).

In natural systems, it is often difficult to determine to what extent fractures in a hydrated rock are related to the far field external stresses rather than the internal stresses generated by the hydration reaction itself (Rouméjon & Cannat, 2014). Experimental investigations under controlled stress conditions are therefore important to better understand how reactions progress under different stress conditions and under what conditions reaction-induced fracturing occurs. In this study, we conducted dynamic microtomography experiments to investigate the effect of confining pressure on the conversion of chemical potential energy to mechanical work required to produce fractures. We consider a case whereby porous periclase (MgO) is hydrated to form brucite ($Mg(OH)_2$). This reaction is believed to represent a relevant analog system similar

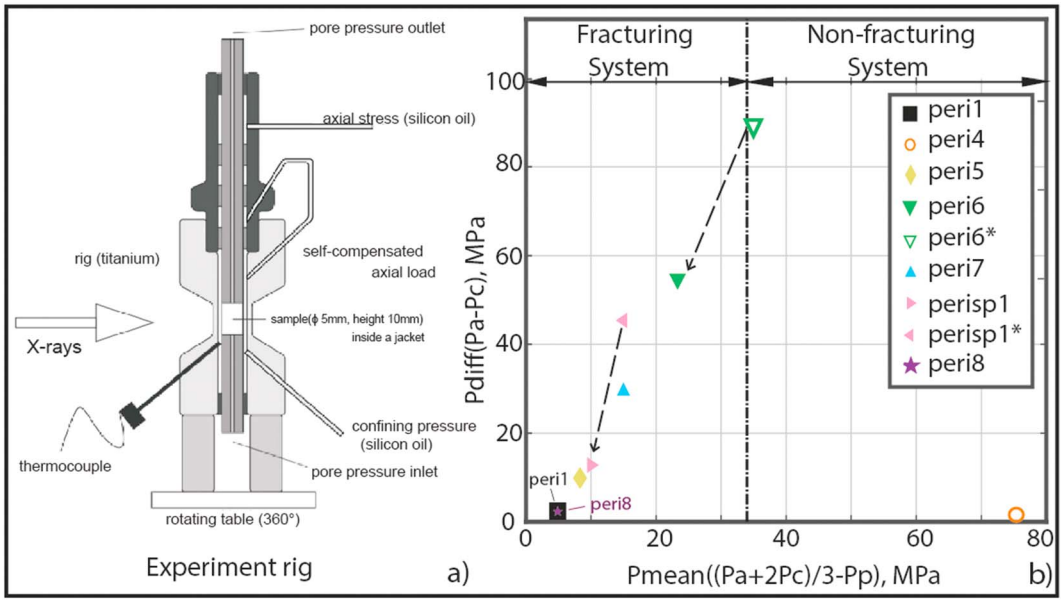

Figure 1. (a) Schematic diagram of the HADES triaxial rig. (b) Stress states (effective mean stress versus differential stress) for all samples (see Table 1). The dashed arrows represent changes of stress states in a sample during reaction. Samples subjected to effective mean stresses less than 30 MPa show intense reaction-induced fracturing.

to many reactions taking place during retrograde metamorphism, including serpentinization. In the oil and gas industry, hydration of cements containing various amounts of calcium or magnesium oxide is often used to efficiently seal boreholes (Wolterbeek et al., 2017). The real-time microscale structural evolution of the periclase sample at in situ stress and temperature conditions were obtained using synchrotron X-ray microtomography. We studied the effect of imposed stresses, including the differential and mean stresses, on reaction rate and reaction-induced fracturing.

2. Materials and Methods

The reaction $MgO + H_2O = Mg(OH)_2$ has an associated solid volume increase of about 110% accompanying a 45% weight increase (Kuleci et al., 2016). The equilibrium temperature of the dehydration reaction of brucite to form periclase is ~550 °C at 1 atm pressure (Johnson & Walker, 1993). The kinetics of this reaction have been studied experimentally (Liu et al., 2017) and follow an Avrami-type sigmoidal kinetics (Avrami, 1939) at temperatures between 320 to 360 °C and pressures ranging from 819 to 1,282 MPa. The hydration of periclase into brucite was studied by Kuleci et al. (2016) under a pressure of 200 MPa and temperatures between 350 to 620 °C for a duration of between 5 and 40 min. In their experiments, a cube of periclase was left in contact with water, and a rim of brucite grew at the surface of the periclase, without fracturing the original periclase crystal.

Here we study the effect of confinement on reaction-induced fracturing during the hydration of periclase (MgO) into brucite ($Mg(OH)_2$). The cylindrical samples of periclase ceramics with well-connected initial porosities between 0.5 to 1.6% have a diameter of 5 mm and a height of 10 mm. Each periclase sample was placed in the triaxial deformation apparatus *HADES* (Renard et al., 2016), where the confining pressure, axial stress, pore fluid pressure, and temperature can be controlled independently (Figure 1). A jacket made of Viton fluoropolymer elastomer encased each sample, separating the confining medium (silicon oil) and the pore fluid (distilled water). HADES is transparent to X-rays and was mounted on the rotating stage of the X-ray tomography beamline ID19 at the European Synchrotron Radiation Facility (ESRF) in Grenoble, France. The progress of the periclase hydration reaction can be imaged at the desired conditions of pressure and temperature using synchrotron radiation time-resolved X-ray computed microtomography.

Table 1
Summary of Experiment Conditions

Test no.	P_a (MPa)	P_c (MPa)	P_p (MPa)	P_{mean} (MPa)	$P_{diff.}$ (MPa)	T (°C)	t (min)	No.
Peri1	11	10	5	5	1	210	120	30
Peri4	81	80	5	75	1	200	180	68
Peri5	20	10	5	8	10	180	90	27
Peri6	100 → 65	10	5	35→23	90→55	180	150 → 180	130
Peri7	40	10	5	15	30	170	300	65
Perisp1	30 → 25 → 50	10 → 5	5	12 → 10 → 15	20 → 15 → 45	180	210	93
Peri8	81	80	75	5	1	180	250	40

Note. P_a, axial stress; P_c, confining pressure; P_p, pore fluid pressure; $P_{mean} = (Pa + 2Pc)/3 - Pp$ effective mean pressure stress; $P_{diff} = P_a - P_c$ differential stress; T, temperature, t, duration of experiment after temperature was stable and water was injected. No., number of tomography scans per experiment.

We performed seven experiments at varying confining pressure Pc, temperature T, and axial stress Pa conditions (Table 1 and Figure 1b). A pore fluid pressure Pp of 5 MPa was used in all but one experiments, in which the pore pressure was at 75 MPa (sample peri8). A small fluid pressure gradient of 0.5 MPa was imposed between the pore fluid inlet and outlet of the sample to drive fluid flow. In the experiments, the axial and confining pressures were imposed first, then the sample was heated at 2°/min until the desired temperature, before the pore fluid pressure was increased to the desired value. In all experiments (Table 1), the same procedure was followed. For each sample, three-dimensional (3-D) tomography volumes were acquired every 5 min during the progress of reaction. The volumes were then reconstructed as 16-bit gray level 3-D images, with a voxel size of 6.5 μm.

All the reconstructed data sets are of excellent quality, with a low level of noise and artifacts. Since X-ray attenuation depends on density and is represented by gray values, the three phases—periclase, brucite, and pores—can easily be separated (Figure 2). The gray value of brucite is very similar to the jacket around the sample; therefore, the background was subtracted with a mask and only the sample was preserved (Figures 3 and 4). For all time steps, we calculated histograms of the gray value frequency distribution from 180 million voxels that constituted a parallelepiped subvolume just off the center of the sample cylinder (Figure 2). As the reaction progressed through the parallelepiped, changes in the volume fraction of periclase, brucite, and porosity were measured (Figure 2). By *pore*, we refer to the definition of Sprunt and Brace (1974) for the pore space that includes both the existing pores of the sample and the newly created pores during the experiments. We separated (i.e., segmented) the three phases after reducing the noise in the data through a nonlocal mean filtering and masking out the sample from the surrounding jacket and background for all the time series.

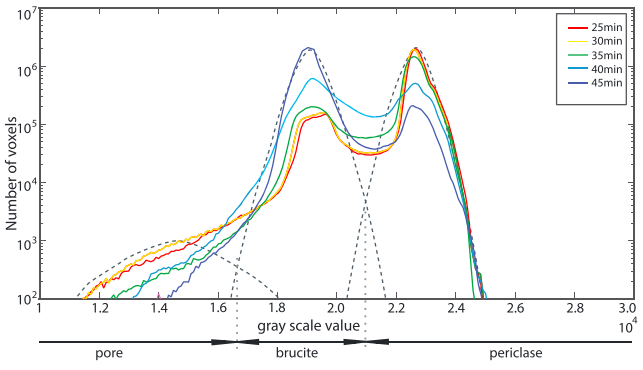

Figure 2. Histograms of gray scale values of the microtomography images of sample peri1 undergoing the periclase to brucite transformation. The histograms (solid curves; different colors represent different reaction time) can be divided into three slightly overlapping bell-shaped curves (dashed lines), which are interpreted as pore space, brucite and periclase, from left to right. Periclase volume fraction decreased, while brucite increases with time as reaction progressed.

All pores in the above-mentioned parallelepiped were extracted. We used the method of Liu et al. (2009) to label face-connected clusters of pore voxels as individual voids and calculated the position, volume, and surface area of each individual pore. Using a cutoff threshold of 10 voxels for pores, we obtained the total volume fraction of periclase, brucite, and porosity of 99.24 to 99.98%. Given the porosity of 1–1.5% from the pores above the cutoff, the contribution of the pores less than 10 voxels could approach 43% of the total porosity. Consider the *large porosity* range from 0.5% to 1.5%, within our error the small pores (smaller than 10 voxels) neglected here represent 0.6% to 33% of the total porosity. Even though this is indeed a nonnegligible fraction, these small pores do not contribute significantly to the permeability. Because the rates of fluid-mineral interactions are directly controlled by the mineral surface area and not all parts of periclase surface were in contact with fluid, we segmented the reactive surface area as the interface between periclase and pore fluid at each time step. To do this, we first extracted the surface areas for periclase,

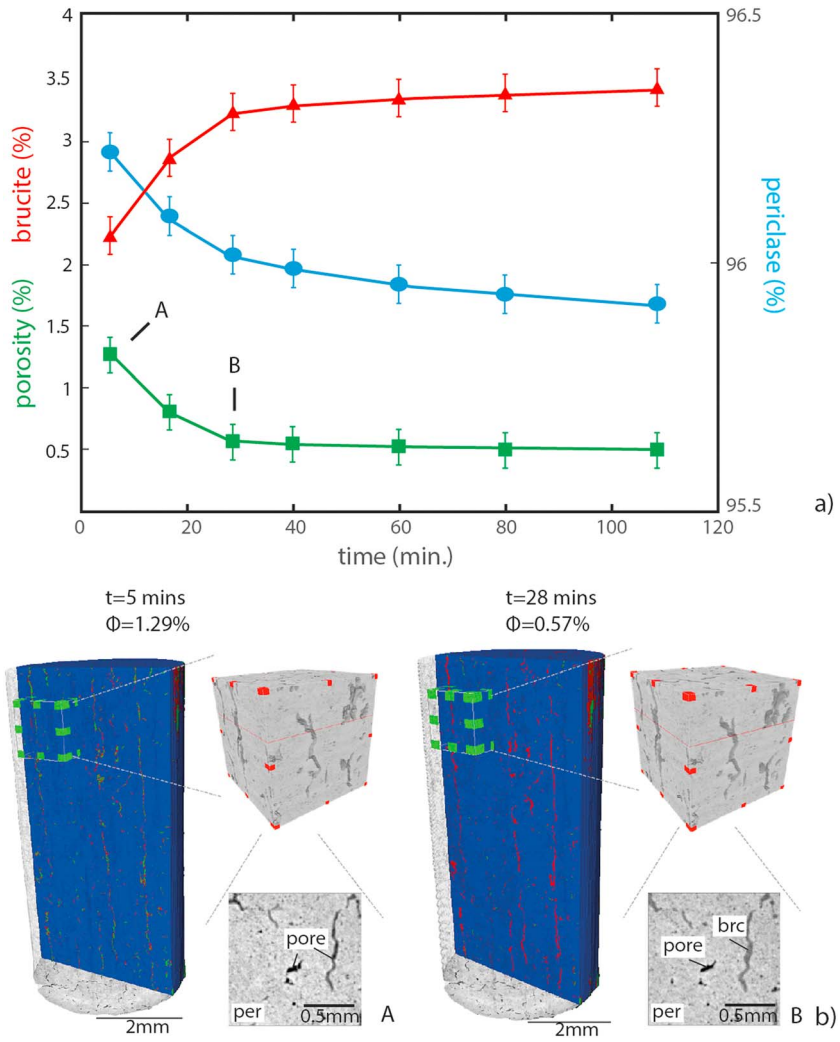

Figure 3. (a) Evolution of porosity (green), volume fractions of brucite (red), and periclase (blue) in sample peri4 at an effective mean stress of 75 MPa. (b) Microstructures of sample peri4 (a) 5 and (b) 28 min after reaction started. In the cross-section view of the whole sample, the initial periclase (per) is dark blue, porosity (pore) is green, and brucite (brc) is red. The 3-D and 2-D images of subvolumes are shown as insets where periclase (per) is light grey, porosity (pore) is dark grey, and brucite (brc) is intermediate grey. Filling of the existing pores with brucite can be observed.

brucite, and pore phases and labeled them. Then we selected the surface area between periclase and pore fluid that we consider to represent the reactive surface area.

3. Results

Extensive reaction-produced fracturing is observed in every sample subjected to an effective mean stress $P_{mean} = (2P_c + P_a)/3 - P_p$ of 30 MPa or less. In contrast, no fracturing was observed in the two experiments with an effective mean stress greater than 30 MPa (P_{mean}, 35 and 75 MPa), regardless the level of differential stresses imposed. The control of effective mean stress on fracturing is well illustrated in sample peri6. At a P_{mean} of 35 MPa and a differential stress $P_{diff} = P_a - P_c$ of 90 MPa (Figure 1b), sample peri6 exhibited no fracturing. However, when the P_{mean} was decreased to 23 MPa by lowering P_{diff} to 65 MPa, the reaction rate was greatly accelerated and fracturing was observed during the time scale of the experiment. In the following we describe the evolution in porosity and phase content for the various experiments.

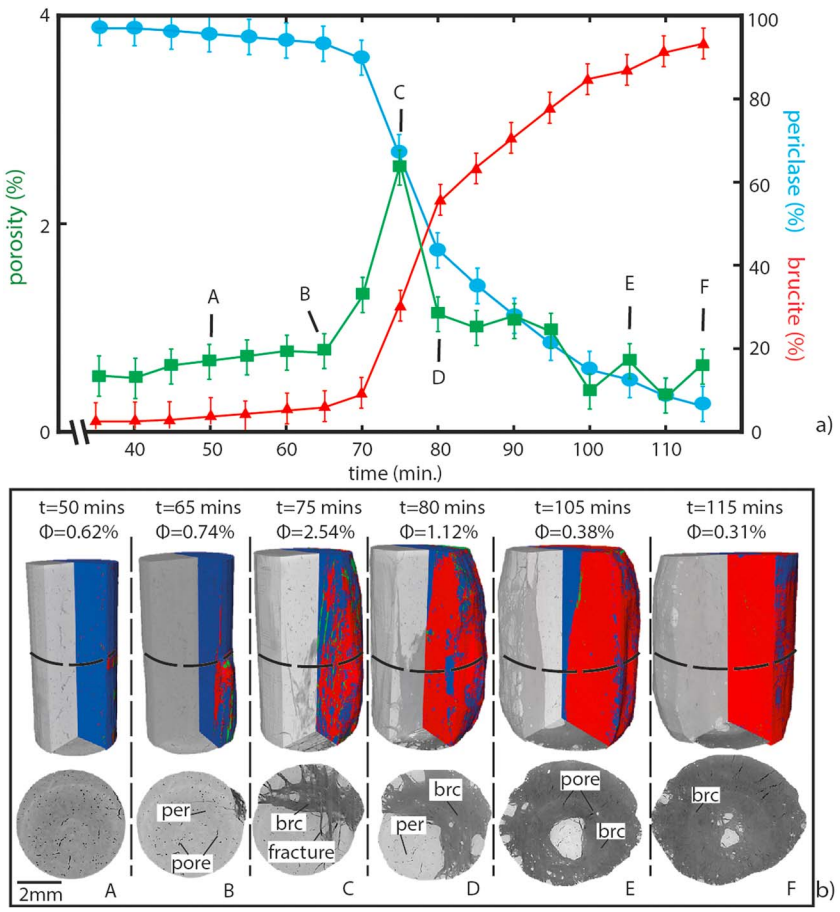

Figure 4. (a) Reaction progress for sample peri1 showing a sigmoidal evolution of brucite-for-periclase replacement. A porosity pulse was observed between 65 to 80 min. (b) Time evolution of peri1 with a (top) 3-D view and (bottom) 2-D cross-section view at the middle of the sample (locations marked by dashed curves). The 3-D views show the X-ray adsorption data in gray scale. The segmented phases are colored (per: periclase, blue; brc: brucite, red; porosity: green).

3.1. Experiments Without Reaction-Induced Fracturing

The hydration progress in sample peri4 at P_{mean} = 75 MPa and P_{diff} = 1 MPa (Figure 3) is very similar to that in sample peri6 at P_{mean} = 35 MPa and P_{diff} = 90 MPa despite the large difference in differential stress. Reaction-induced fracturing was not observed in either experiment. The evolution of porosity in a subvolume composed of 250 × 250 × 250 voxels (or 1625 μm × 1625 μm × 1625 μm) is shown in Figure 3b.

Over the first 40 min, the total porosity in peri4 decreased from an initial value of 1.3% to a constant value of 0.5%. Large pores are preferentially filled by brucite (Figure 5). After 110 min about 3.5 vol.% of brucite was formed, and more than 3 vol.% appeared during the first 30 min. This suggests that the existing pores were clogged and without reaction-induced fracturing the reaction progress is very slow.

3.2. Experiments With Reaction-Induced Fracturing

Six experiments were conducted at a mean stress below 30 MPa (Figure 1b and Table 1). Three of them (peri7, peri8, and perisp1) were performed to check reproducibility of results and confirm the fracturing limit of effective mean stress at 30 MPa. Most experiments were conducted at a confining pressure of 10 MPa and differential stresses of 6 MPa (peri1; Figure 4), 15 MPa (peri5; Figure S1), and 60 MPa (peri6; Figure 7). One experiment (peri8) was conducted at high confining pressure (80 MPa) and high pore fluid pressure (75 MPa). Detailed analyses show that in all these experiments, the replacement of periclase to brucite is a sigmoid function of time. After a slow start (stage 1), the rate of replacement picks up accompanied by

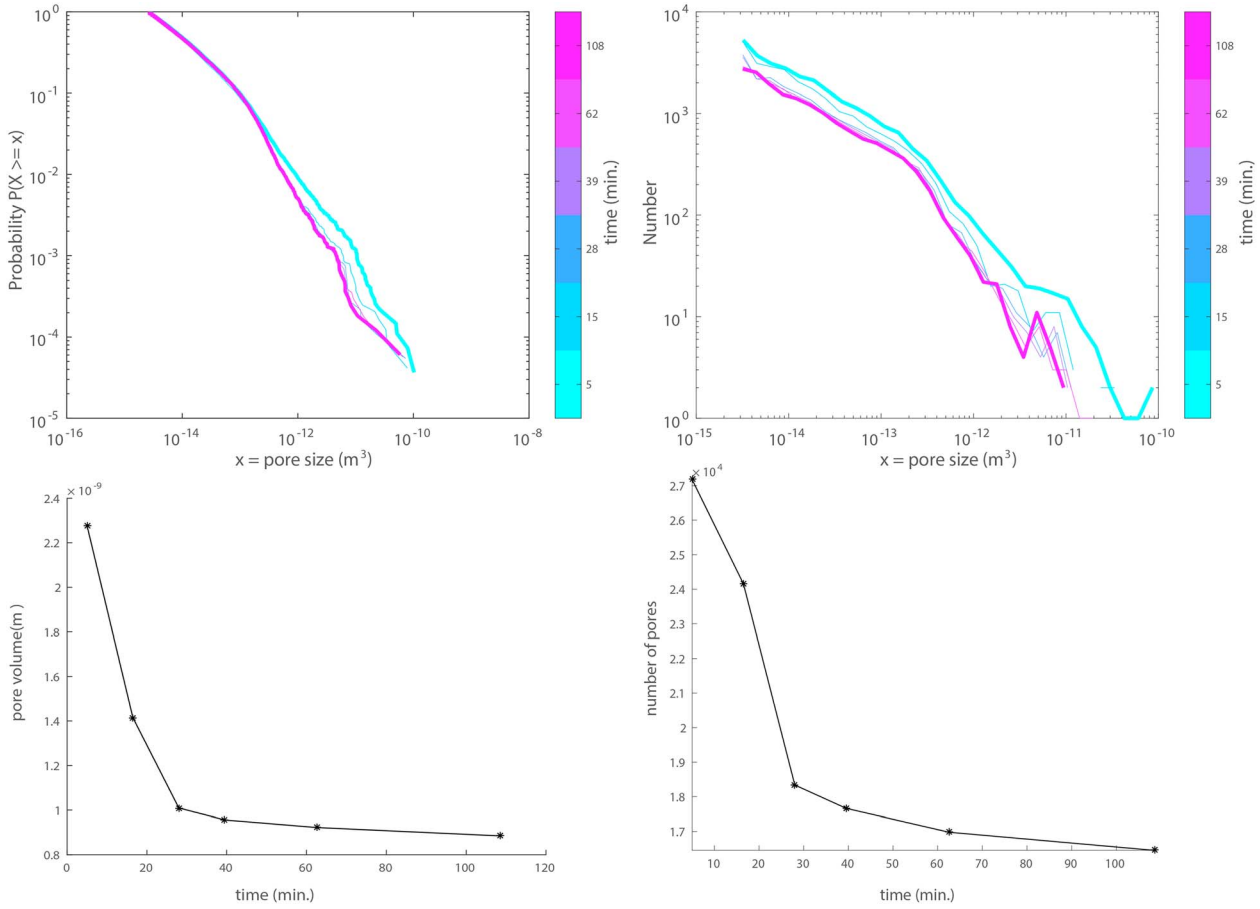

Figure 5. Pore size distribution in a subvolume of sample peri4. (a) Probability that a pore X has a size (i.e., volume) larger than *x*. (b) Histogram of pore volume. (c) Evolution of total pore volume with time. (d) Total number of pores detected as reaction progresses. All these data show that initial pores become filled with brucite and both their number, size, and total volume decrease. The cyan to magenta color transition represents the increasing reaction time.

intense fracturing and a pulse-like porosity increase (stage 2). In stage 3, the rate gradually declines till the replacement is complete (Figure 4).

For sample peri1 (Figure 4 and Video S1), brucite is barely visible after 20 min (stage 1) and becomes obvious after 30 min (onset of stage 2). At about 35 min, the reaction rate accelerates at the onset of global fracturing. At 45 min a maximum porosity of ~2.5% is reached. After that the reaction slows down gradually and the pore space is quickly reduced to less than 1% (stage 3). After 85 min, the reaction is about 95% complete in terms of periclase consumption. The pore size distribution (Figure 6) shows an evolution where the porosity pulse corresponds to an increasing and then decreasing number of pores. The reduction in porosity is associated with interconnection of previously isolated pores.

In sample peri5 (Figures S1 and S2 and Video S2), fracturing and brucite formation can be observed after 25 min (onset of stage 2), then it follows a reaction pattern similar to the one in peri1. Again, the porosity increase is pulse-like, first increasing to ~2.1% and then decreasing. The microstructure that formed during the intermediate stages of reaction progress (stage 3) is remarkably similar to the so-called mesh textures that often develop during serpentinization of olivine-rich rocks (Jamtveit et al., 2009; O'Hanley, 1992; Wicks & Whittaker, 1977). Again, the reaction is nearly complete after 90 min.

At P_{mean} of 23 MPa and P_{diff} of 65 MPa, sample peri6 was subjected to higher stresses than samples peri1 and peri5 (Figure 1b). The initial porosity of peri6 was also higher (ϕ = 1.65%). In this case, the transition between stage 1 and 2 took only 10 min. In stage 2 both the progress of the reaction and the development of a porosity pulse are slower in peri6 than in the previous cases (Figure 7). The porosity does however reach a much

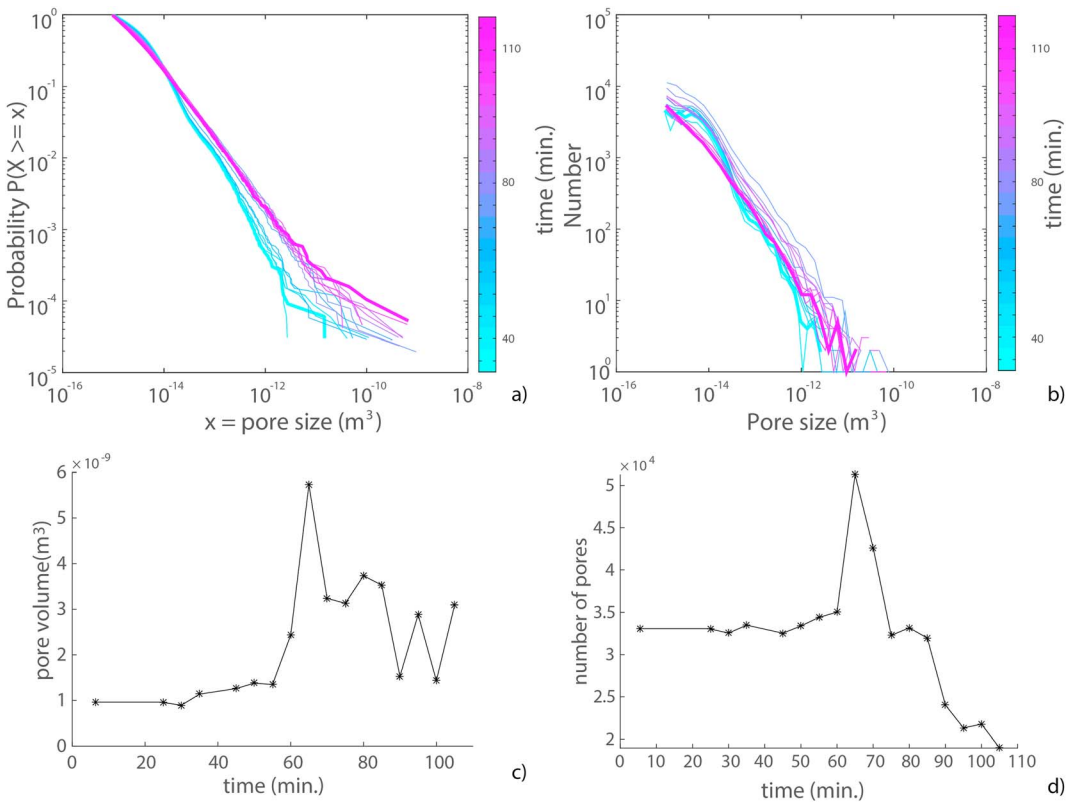

Figure 6. Pore size distribution of sample peri1. (a) Probability that a pore X has a size (i.e., volume) larger than *x*. (b) Histogram of pore volume. (c) Evolution of total pore volume with time. (d) Total number of pores detected as reaction progresses. All these data show that initial pores become filled with brucite and both their number, size, and total volume decreases. The cyan to magenta color transition represents the increasing reaction time.

higher value (~12.5%) at around 90 min. After 140 min, there is still 20% periclase left and the reaction rate is still significant. For peri8, which was conducted at high confining pressure (80 MPa) and high pore fluid pressure (75 MPa), fracturing started from around 120 min and the reaction was approximately 80% complete after 250 min.

The experimental results suggest that the brucite growth in the pore space of the porous periclase produces reaction-induced fracturing only if the effective mean stress is less than 30 MPa either at low confining pressures or at high confining pressures but with a pore fluid pressure close to the confining pressure. When the hydration reaction takes place under higher effective mean stresses, brucite growth clogs the existing pores and causes a substantial reduction of the global reaction rate. Detailed inspection of the pore size statistics (Figures 5, 6, and S2) shows that the reaction product (i.e., brucite) preferentially fills the largest pores.

4. Discussion and Conclusions

Brucite growth clearly produces fracturing during experiments conducted at low effective mean stress, and the volume increase of brucite is an approximately sigmoidal function of time. After a slow start, the brucite growth rate accelerates at the onset of fracturing and slows down as the system is running out of reacting periclase (Figures 4, 7, and S1). This behavior resembles an Avrami type kinetics where the initial stage is slow due to slow nucleation and the reaction rate follows a bell-shaped curve when plotted versus time. The Avrami kinetics model (Avrami, 1939) describes the relationship between the transformed volume fraction $X(t)$ and time t according to the equation $X(t) = 1 - \exp(-kt^n)$, where k is the reaction rate in s^{-n} and n is a time exponent that depends on the reaction mechanism. This equation can be linearized after taking the logarithm two times, to give $\ln(-\ln[1 - X(t)]) = \ln k + n \ln t$, which produces a sigmoidal reaction progress, as observed in our experiments.

We define the reaction rate as $R = \Delta V/\Delta t$ where ΔV represents for the increase in brucite volume or the decrease in periclase volume. Our data do not follow a simple Avrami model due to the large volume

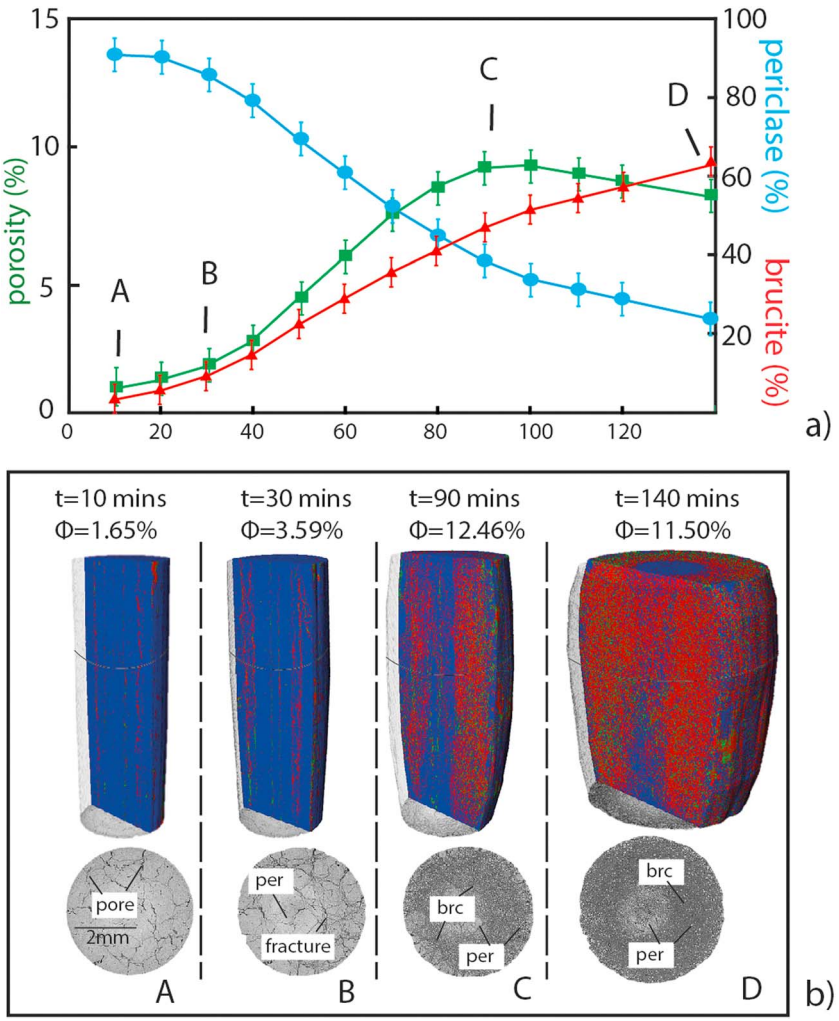

Figure 7. (a) Reaction progress for sample peri6 showing a sigmoidal evolution of brucite-for-periclase replacement. A porosity pulse was observed between 45 to 120 min. (b) Time evolution of peri6 with a (top) 3-D view and (bottom) 2-D cross-section view at the middle of the sample (locations marked by dashed curves). The 3-D views show the X-ray adsorption data in gray scale. The segmented phases are colored (per: periclase, blue; brc: brucite, red; porosity: green).

increase involved. However, the bell-shaped Avrami rate has in many respects an analog in the *porosity pulse* observed in these experiments. This pulse reflects the evolution of reactive surface area largely generated by the fracturing process and thus also reflects the evolution in reaction rate. The reduction in porosity observed during the last stages of the experiments results from clogging of cracks and pores when the rate of the fracture generating reaction ($MgO + H_2O = Mg(OH)_2$) decreases. Zhang et al. (1994) proposed that the pore closure could be related to plastic deformation (i.e., pore collapse) due to stress concentration at the pore walls. Because our dynamic microtomography data show no evidence of pore collapsing, we conclude that porosity reduction observed in our experiments is mainly due to pore clogging.

The reaction transforms periclase into brucite with a volume expansion of 110%. This expansion increases the pore volume by fracturing. At the same time, some pores become clogged because of the precipitation of brucite. The volume of the sample, V_{sample}, evolves as a function of time according to

$$(1 - \phi(t))V_{sample}(t) = n_{pe}(t)\overline{V}_{pe} + n_{br}(t)\overline{V}_{br} \quad (1)$$

where n_{pe} and n_{br} are the number of moles of periclase and brucite, respectively, $\overline{V}$ (m^3/mol) is a molar volume, and ϕ is the porosity. As a consequence, porosity varies according to a partial differential equation:

$$(1-\phi(t))\frac{dV_{sample}(t)}{dt} - V_{sample}(t)\frac{d\phi(t)}{dt} = \frac{dn_{pe}(t)}{dt}\overline{V}_{pe} + \frac{dn_{br}(t)}{dt}\overline{V}_{br} \quad (2)$$

The net porosity change is determined by two mechanically coupled processes, the formation of fracture and the clogging of pores:

$$\frac{d\phi}{dt} = \frac{d\phi_{frac}}{dt} + \frac{d\phi_{clogging}}{dt} \quad (3)$$

where $d\phi_{frac}$ is the porosity change due to the formation of fractures and $d\phi_{clogging}$ is the porosity change due to precipitation of brucite that clog the pores because of its higher molar volume than periclase. The resolution of the system of equations (2) and (3) requires numerical modeling of the coupling between the Avrami kinetics of the periclase to brucite reaction that controls volume expansion and mechanical modeling of fracture formation. Such modeling could be performed using, for example, a discrete element modeling approach (Ulven, Jamtveit, & Malthe-Sørenssen, 2014; Ulven, Storheim, et al., 2014), but is out of the scope of the present study. Aharonov et al. (1997) simulated crystallization during reactive fluid flow into porous rock. They demonstrated that crystallization preferentially took place within fluid pathways with high permeability, gradually changing a well-connected channelized network to a disconnected, more random, distribution of pores. In our experiments a similar effect can be expected, in addition to the deformation due to volume expansion of the transformation of periclase into brucite.

The reaction in sample peri6 was carried out at high mean and differential stress (23 and 65 MPa, respectively), and this experiment shows a different evolution than the ones described above. An initial period of gradual increase in the reaction rate and associated porosity growth, to a very high porosity of 12.5%, is followed by a reduction in reaction rate. This reduction in reaction rate takes place while the porosity is still increasing and the progress of reaction has reached only about 20% periclase consumption. The reaction and fracturing in sample peri6 (Figure 7a) proceeded slower than for samples peri1 (Figure 4a) and peri5 (Figure S1a). Because sample peri6 has a higher porosity than other samples, the slower reaction rate cannot be due to limited fluid supply or low reactive surface area. A possible explanation could be that the rate of brucite growth in the periclase pores or fractures is slower in this case. Since, all experiments are conducted at broadly similar temperature and pressure conditions, this effect is not due to differences in the thermodynamic affinity of the brucite-forming reaction, which is very high in all cases. A *force of crystallization* σ_{foc}, equivalent to the pressure required to stop the reaction by pushing it toward equilibrium, can be calculated from Eq. 13 of Kelemen and Hirth (2012) and also derived in Wolterbeek et al. (2017):

$$\sigma_{foc} = \frac{\Delta_f G^{P,T}_{MgO} + \Delta_f G^{P,T}_{H_2O} - \Delta_f G^{P,T}_{Mg(OH)_2}}{V^{P,T}_{m,Mg(OH)_2} - V^{P,T}_{m,MgO}}. \quad (4)$$

Taking the Gibbs free energies of formation of periclase, brucite, and water at 200 °C equal to −550, −785, and −210 kJ/mol, respectively, and the molar volumes of periclase and brucite (11.248 and 24.630 cm^3/mol, respectively), the expected force of crystallization is ~1.9 GPa. The variation of Gibbs free energy due to the creation of surface area is defined as $\gamma\left(\frac{\partial G}{\partial A}\right)_{T,P}$, where γ is the surface energy and A is the surface area. Surface tension of MgO has been measured by Jura and Garland (1952), who found values of the order of 1.05 J/m^2. For brucite we did not find surface tension data, and we assume a value of the same order as for periclase. The contribution of the surface energy to the Gibbs free energy for particles of radius r = 1 micrometer size, and given the molar volume of periclase $\overline{V}_{pe} = 11.62\ 10^{-6}$ m^3/mol is $\Delta G_\gamma = \frac{2\gamma}{r}\overline{V}_{pe}$ = 23 J/mol. Compared to the driving force related to the phase transformation from periclase to brucite, of the order of 25 kJ/mol, the effect of surface tension is small and we neglected it in the calculation of the force of crystallization.

However, our experimental results show that an effective mean stress of only 30 MPa, less than 2% of the theoretical force of crystallization, may be sufficient to prevent reaction-induced fracturing during the course of our experiments and slow down the reaction rate. A similar lack of reaction produced fractures is also observed during serpentinization and carbonation of single grains of olivine (Hövelmann et al., 2012), another system in which the force of crystallization is expected to be hundreds of MPa (e.g., Kelemen & Hirth, 2012). One possible explanation for this observation is that the reduction in the rate of the brucite-forming reaction is due to a change in the structure of the reactive periclase-water-brucite interface itself.

For the brucite forming reaction to progress where brucite simultaneously exerts a pressure on the confining periclase, a fluid film must be able to remain stable at the periclase-brucite interface even when subject to significant normal stress (Renard & Ortoleva, 1997; Scherer, 2004). This requires that the close range hydration forces between the brucite and periclase interface in the presence of a fluid film are repulsive, as is observed in a number of other systems such as the calcite-calcite interfaces (Røyne et al., 2011; Røyne & Jamtveit, 2015). If, however, the normal stress exceeds the repulsion forces, the fluid film thickness will be reduced down to one or two layers of water molecules (Renard & Ortoleva, 1997). As a consequence, transport of water along grain boundaries will slow down, the reaction will slow down as well. This level of normal stress is often referred to as the disjoining pressure (De Gennes, 1985; Derjaguin & Churaev, 1974).

The disjoining pressure describes the physics of wetting or dewetting of a liquid film on a solid surface. It is the negative derivative of the free energy with respect to film thickness (Derjaguin & Churaev, 1974). The disjoining pressure arises from the interaction energies of molecules in a film being different from that in the bulk. The energy contributions to the energy of thin films could have different origins: surface curvature (Steiger, 2005), osmotic effect due to surface charges at the mineral surfaces (Renard & Ortoleva, 1997), van der Waals forces acting between the film and the mineral surface, or polar interactions between water molecules near the mineral surface that are different from bulk water. Because several effects are involved, parameters that are likely to control the disjoining pressure are mineral surface charge, salinity of the fluid, curvature of the solid surface, and temperature. Despite a variety of processes involved, the net effect of disjoining pressure is that it induces an excess fluid pressure within a grain contact, compared to the pore fluid (Scherer, 2004). If the stress loading two grains increases, the resulting effect is to squeeze out the film at the contact. When the total pressure in the thin film overcomes the pore pressure plus the disjoining pressure, water should be expelled, producing a dry contact. The rate of a fluid-consuming reaction will be reduced in a system where the local normal stress at the reactive interfaces approaches the relevant disjoining pressure. We thus infer that at an effective mean stress of 30 MPa, the periclase-brucite system is approaching a situation where the normal stresses at the reacting interfaces approach the disjoining pressure, and the rate of reaction will slow down, even if the porosity in the system is still high. It is the interfacial forces at the reactive surface that dictate the behavior of the system, and not the theoretical thermodynamic pressure required to push the reaction toward equilibrium.

Because brucite is a mechanically weak phyllosilicate mineral, the lack of reaction-induced fracturing at effective stress $>$35 MPa could also have resulted from relaxation of crystallization pressure via viscous creep and via frictional sliding along existing fractures or cleavage planes. Taking the flow law of muscovite, a weak mineral, derived by Mariani et al. (2006) at 200 °C and 30 MPa effective stress, the viscous creep during the time scale of our experiments would be insignificant. Relaxation of crystallization pressure via frictional sliding is not consistent with our experimental results.

Here we compare the two experiments PERI1 and PERI4 conducted at the same different stress of 1 MPa (Table 1). Frictional sliding along the preexisting fractures or cleavages obeys the Coulomb-Mohr failure criterion. In PERI1, the maximum effective principal stress is 6 MPa, and the intermediate and minimum effective principal stresses are 5 MPa, which give an effective mean stress of ~5.5 MPa. Taking a friction coefficient for brucite of ~0.3 (Moore & Lockner, 2004, 2005, 2007), the yield strength is roughly ~1.6 MPa for PERI1. With a differential stress of 1 MPa applied to sample PERI1, it is conceivable that frictional sliding could contribute to the relaxation of crystallization pressure.

In comparison, in PERI4, the maximum effective principal stress is 76 MPa, and the intermediate and minimum effective principal stresses are 75 MPa, which give an effective mean stress of ~75.5 MPa. Thus, the yield strength of PERI4 is ~22.6 MPa. With a differential stress of 1 MPa for PERI4, relaxation via frictional sliding in PERI4 is unlikely. If relaxation via frictional sliding was the mechanism that inhibited fracturing, then more fracturing should be expected in PERI4 than in PERI1, which is opposite to the observation. Therefore, we conclude that the low shear strength of brucite cannot explain the difference in the rate of periclase transformation that we observed.

In the case of a higher differential stress, the formation of brucite along well-defined planes could induce shear faulting because of the small friction of this mineral. This mechanism has been proposed to explain the weakness of large continental faults (Moore & Lockner, 2007). However, we did not observe shear faulting in our experiments conducted with a differential stress of 45 or 55 MPa (see Table 1). We cannot rule out,

however, that experiments performed at high differential stress, while keeping a confining pressure below 30 MPa, could produce shear faulting where the low shear strength of brucite would play a role in controlling the rate of periclase transformation.

These results are relevant to common geological systems, such as the hydration of olivine-rich rocks to form variably serpentinized product rocks. The microstructures produced during serpentinization are often strikingly similar to those observed in the experiments described above (Figures 4b and 7b) and may reflect a similar reaction-driven fracturing mechanism as serpentinization is associated with a solid volume increase of 30–55% (MacDonald & Fyfe, 1985; O'Hanley). At temperatures around 200 °C, thermodynamic consideration suggests that serpentinization should be able to produce stresses exceeding 300 MPa (Kelemen & Hirth, 2012) and thus be able to crack rocks to a depth of several kilometers in the Earth's lithosphere. However, complete serpentinization is uncommon in rocks that have not been subject to penetrative shear deformation. This observation is usually ascribed to clogging of the pore space due to the solid volume increase, which would limit fluid supply, like observed in samples peri4 and peri6 in this study. Whether such clogging effects are affected by interface properties such as the disjoining pressure for the olivine-serpentine couple or merely is an effect of the bulk transport properties of the partly serpentinized peridotite is not known and would be an interesting topic of further field and laboratory studies.

Acknowledgments
The deformation apparatus was built by Sanchez Technology. This study received funding from the Norwegian Research Council (project HADES, grant 250661 to F. R.) and the European Union (H2020 ERC Advanced Grant Agreement 669972, "Disequilibrium Metamorphism" to B. J.); beamtime was allocated at the European Synchrotron Radiation Facility (Long Term Proposal ES-295). Data storage was provided by UNINETT Sigma2—the National Infrastructure for High Performance Computing and Data Storage in Norway (project NS9073K). W. Z. was partially supported by the U. S. National Science Foundation through EAR-1551300. Maya Kobchenko is thanked for the help provided to analyze the tomography data. We thank Peter Kelemen and one anonymous referee who provided constructive reviews that helped improving the article.

References

Aharonov, E., Spiegelman, M., & Kelemen, P. (1997). Three-dimensional flow and reaction in porous media: Implications for the Earth's mantle and sedimentary basins. *Journal of Geophysical Research*, *102*, 14,821–14,833. https://doi.org/10.1029/97JB00996

Avrami, M. (1939). Kinetics of phase change. I. General theory. *The Journal of Chemical Physics*, *7*(12), 1103–1112. https://doi.org/10.1063/1.1750380

De Gennes, P.-G. (1985). Wetting: Statics and dynamics. *Reviews of Modern Physics*, *57*(3), 827–863. https://doi.org/10.1103/RevModPhys.57.827

Derjaguin, B. V., & Churaev, N. V. (1974). Structural component of disjoining pressure. *Journal of Colloid and Interface Science*, *49*(2), 249–255. https://doi.org/10.1016/0021-9797(74)90358-0

Fletcher, R., Buss, H., & Brantley, S. (2006). A spheroidal weathering model coupling porewater chemistry to soil thicknesses during steady-state denudation. *Earth and Planetary Science Letters*, *244*(1–2), 444–457. https://doi.org/10.1016/j.epsl.2006.01.055

Gratier, J.-P., Frery, E., Deschamps, P., Røyne, A., Renard, F., Dysthe, D., & Hamelin, B. (2012). How travertine veins grow from top to bottom and lift the rocks above them: The effect of crystallization force. *Geology*, *40*(11), 1015–1018. https://doi.org/10.1130/G33286.1

Hövelmann, J., Putnis, C., Ruiz-Agudo, E., & Austrheim, H. (2012). Direct nanoscale observations of CO2 sequestration during brucite [$Mg(OH)_2$] dissolution. *Environmental Science & Technology*, *46*(9), 5253–5260. https://doi.org/10.1021/es300403n

Jamtveit, B., & Hammer, Ø. (2012). Sculpting of rocks by reactive fluids. *Geochemical Perspectives*, *1*(3), 341–481. https://doi.org/10.7185/geochempersp.1.3

Jamtveit, B., Malthe-Sørenssen, A., & Kostenko, O. (2008). Reaction enhanced permeability during retrogressive metamorphism. *Earth and Planetary Science Letters*, *267*(3-4), 620–627. https://doi.org/10.1016/j.epsl.2007.12.016

Jamtveit, B., Putnis, C. V., & Malthe-Sørenssen, A. (2009). Reaction induced fracturing during replacement processes. *Contributions to Mineralogy and Petrology*, *157*(1), 127–133. https://doi.org/10.1007/s00410-008-0324-y

Johnson, M. C., & Walker, D. (1993). Brucite [$Mg(OH)_2$] dehydration and the molar volume of H_2O to 15 GPa. *American Mineralogist*, *78*(3–4), 271–284.

Jura, G., & Garland, C. W. (1952). The experimental determination of the surface tension of magnesium oxide. *Journal of the American Chemical Society*, *74*(23), 6033–6034. https://doi.org/10.1021/ja01143a062

Kelemen, P. B., & Hirth, G. (2012). Reaction-driven cracking during retrograde metamorphism: Olivine hydration and carbonation. *Earth and Planetary Science Letters*, *345*, 81–89.

Kelemen, P. B., & Matter, J. (2008). In situ carbonation of peridotite for CO_2 storage. *Proceedings of the National Academy of Sciences*, *105*(45), 17,295–17,300. https://doi.org/10.1073/pnas.0805794105

Kelemen, P. B., Matter, J., Streit, E. E., Rudge, J. F., Curry, W. B., & Blusztajn, J. (2011). Rates and mechanisms of mineral carbonation in peridotite: Natural processes and recipes for enhanced, in situ CO_2 capture and storage. *Annual Review of Earth and Planetary Sciences*, *39*(1), 545–576. https://doi.org/10.1146/annurev-earth-092010-152509

Kuleci, H., Schmidt, C., Rybacki, E., Petrishcheva, E., & Abart, R. (2016). Hydration of periclase at 350 °C to 620 °C and 200 MPa: Experimental calibration of reaction rate. *Mineralogy and Petrology*, *110*(1), 1–10. https://doi.org/10.1007/s00710-015-0414-2

Liu, C., Wang, D., Zheng, H., & Liu, T. (2017). A dehydroxylation kinetics study of brucite $Mg(OH)_2$ at elevated pressure and temperature. *Physics and Chemistry of Minerals*, *44*(4), 297–306. https://doi.org/10.1007/s00269-016-0857-y

Liu, J., Regenauer-Lieb, K., Hines, C., Liu, K., Gaede, O., & Squelch, A. (2009). Improved estimates of percolation and anisotropic permeability from 3-DX-ray microtomography using stochastic analyses and visualization. *Geochemistry, Geophysics, Geosystems*, *10*, Q05010. https://doi.org/10.1029/2008GC002358

Macdonald, A., & Fyfe, W. (1985). Rate of serpentinization in seafloor environments. *Tectonophysics*, *116*(1–2), 123–135. https://doi.org/10.1016/0040-1951(85)90225-2

Malvoisin, B., Brantut, N., & Kaczmarek, M.-A. (2017). Control of serpentinisation rate by reaction-induced cracking. *Earth and Planetary Science Letters*, *476*, 143–152. https://doi.org/10.1016/j.epsl.2017.07.042

Mariani, E., Brodie, K. H., & Rutter, E. H. (2006). Experimental deformation of muscovite shear zones at high temperatures under hydrothermal conditions and the strength of phyllosilicate-bearing faults in nature. *Journal of Structural Geology*, *28*(9), 1569–1587. https://doi.org/10.1016/j.jsg.2006.06.009

Moore, D., & Lockner, D. (2005). *Solution-transfer processes and the frictional strength of heated brucite*. Paper presented at the AGU Fall Meeting Abstracts.

Moore, D. E., & Lockner, D. A. (2004). Crystallographic controls on the frictional behavior of dry and water-saturated sheet structure minerals. *Journal of Geophysical Research*, *109*, B03401. https://doi.org/10.1029/2003JB002582

Moore, D. E., & Lockner, D. A. (2007). Comparative deformation behavior of minerals in serpentinized ultramafic rock: Application to the slab-mantle interface in subduction zones. *International Geology Review*, *49*(5), 401–415. https://doi.org/10.2747/0020-6814.49.5.401

Noiriel, C., Renard, F., Doan, M.-L., & Gratier, J.-P. (2010). Intense fracturing and fracture sealing induced by mineral growth in porous rocks. *Chemical Geology*, *269*(3-4), 197–209. https://doi.org/10.1016/j.chemgeo.2009.09.018

Oelkers, E. H., Gislason, S. R., & Matter, J. (2008). Mineral carbonation of CO_2. *Elements*, *4*(5), 333–337. https://doi.org/10.2113/gselements.4.5.333

O'Hanley, D. S. (1992). Solution to the volume problem in serpentinization. *Geology*, *20*(8), 705–708. https://doi.org/10.1130/0091-7613(1992)020<0705:STTVPI>2.3.CO;2

Renard, F., Cordonnier, B., Dysthe, D. K., Boller, E., Tafforeau, P., & Rack, A. (2016). A deformation rig for synchrotron microtomography studies of geomaterials under conditions down to 10 km depth in the Earth. *Journal of Synchrotron Radiation*, *23*(4), 1030–1034. https://doi.org/10.1107/S1600577516008730

Renard, F., & Ortoleva, P. (1997). Water films at grain-grain contacts: Debye-Hückel, osmotic model of stress, salinity, and mineralogy dependence. *Geochimica et Cosmochimica Acta*, *61*(10), 1963–1970. https://doi.org/10.1016/S0016-7037(97)00036-7

Rouméjon, S., & Cannat, M. (2014). Serpentinization of mantle-derived peridotites at mid-ocean ridges: Mesh texture development in the context of tectonic exhumation. *Geochemistry, Geophysics, Geosystems*, *15*, 2354–2379. https://doi.org/10.1002/2013GC005148

Røyne, A., & Jamtveit, B. (2015). Pore-scale controls on reaction-driven fracturing. *Reviews in Mineralogy and Geochemistry*, *80*(1), 25–44. https://doi.org/10.2138/rmg.2015.80.02

Røyne, A., Meakin, P., Malthe-Sørenssen, A., Jamtveit, B., & Dysthe, D. (2011). Crack propagation driven by crystal growth. *EPL (Europhysics Letters)*, *96*(2), 24003. https://doi.org/10.1209/0295-5075/96/24003

Rudge, J. F., Kelemen, P. B., & Spiegelman, M. (2010). A simple model of reaction-induced cracking applied to serpentinization and carbonation of peridotite. *Earth and Planetary Science Letters*, *291*(1–4), 215–227. https://doi.org/10.1016/j.epsl.2010.01.016

Scherer, G. W. (1999). Crystallization in pores. *Cement and Concrete Research*, *29*(8), 1347–1358. https://doi.org/10.1016/S0008-8846(99)00002-2

Scherer, G. W. (2004). Stress from crystallization of salt. *Cement and Concrete Research*, *34*(9), 1613–1624. https://doi.org/10.1016/j.cemconres.2003.12.034

Sprunt, E. S., & Brace, W. (1974). *Direct observation of microcavities in crystalline rocks*. Paper presented at the International Journal of Rock Mechanics and Mining Sciences & Geomechanics Abstracts.

Steiger, M. (2005). Crystal growth in porous materials—I: The crystallization pressure of large crystals. *Journal of Crystal Growth*, *282*(3–4), 455–469. https://doi.org/10.1016/j.jcrysgro.2005.05.007

Ulven, O., Jamtveit, B., & Malthe-Sørenssen, A. (2014). Reaction-driven fracturing of porous rock. *Journal of Geophysical Research: Solid Earth*, *119*, 7473–7486. https://doi.org/10.1002/2014JB011102

Ulven, O., Storheim, H., Austrheim, H., & Malthe-Sørenssen, A. (2014). Fracture initiation during volume increasing reactions in rocks and applications for CO_2 sequestration. *Earth and Planetary Science Letters*, *389*, 132–142. https://doi.org/10.1016/j.epsl.2013.12.039

Wicks, F., & Whittaker, E. (1977). Serpentine textures and serpentinization. *Canadian Mineralogist*, *15*(4), 459–488.

Wolterbeek, T. K., van Noort, R., & Spiers, C. J. (2017). Reaction-driven casing expansion: Potential for wellbore leakage mitigation. *Acta Geotechnica*, 1–26. https://doi.org/10.1007/s11440-017-0533-5

Zhang, S., Cox, S. F., & Paterson, M. S. (1994). The influence of room temperature deformation on porosity and permeability in calcite aggregates. *Journal of Geophysical Research*, *99*, 15,761–15,775. https://doi.org/10.1029/94JB00647

Zhu, W., Fusseis, F., Lisabeth, H., Xing, T., Xiao, X., De Andrade, V., & Karato, S. i. (2016). Experimental evidence of reaction-induced fracturing during olivine carbonation. *Geophysical Research Letters*, *43*, 9535–9543. https://doi.org/10.1002/2016GL070834